Supporting Information for

Biexciton Binding Energy and Linewidth of Single Quantum Dots at Room Temperature

Sander J.W. Vonk [1], *Bart A.J. Heemskerk* [1], *Robert C. Keitel* [2], *Stijn O.M. Hinterding* [1], *Jaco J. Geuchies* [3], *Arjan J. Houtepen* [3], *Freddy T. Rabouw* [1*]

[1]Debye Institute, Utrecht University, Princetonplein 1,The Netherlands

[2]Optical Materials Engineering Laboratory, ETH Zurich, Leonhardstrasse 21, 8092, Switzerland

[3]Opto-Electronic Materials Section, Faculty of Applied Sciences, Delft University of Technology, van der Maasweg 9, 2629 HZ Delft, The Netherlands

[*] Corresponding Author: f.t.rabouw@uu.nl

S1 Synthesis and characterization of core–shell–shell quantum dots

S1.1 CdSe core synthesis

The synthesis of the CdSe cores was based on a method by Chen et al.[S1] Octadecylphosphonic acid (ODPA, 280 mg), trioctylphosphine oxide (TOPO, 3 g), and cadmium oxide (CdO, 60 mg) were added to a three-neck flask (50 mL) and degassed for one hour at 150°C. The temperature was raised to 320°C and trioctylphosphine (TOP, 1 mL) was added. The mixture was heated to 380°C, and a selenium precursor (Se 60 mg in 0.5 mL TOP) was injected to initiate the core growth. Core growth was allowed to continue for approximately 25 s. The synthesized cores were washed with methyl acetate (1:1 volume ratio), centrifuged, and redispersed in hexane. The product was filtered (Millipore filters 0.2 μm) and the washing steps described above were repeated once. The sample was stored in a glovebox.

S1.2 CdS and ZnS shell growth

To produce the Cd-oleate precursor, Cd-$(acetate)_2$ (1.32 g) was dissolved in octadecene (ODE, 52.4 g) and oleic acid (OA, 7.4 g) and heated to 120°C for three hours. After three hours, the Cd-oleate solution was cooled down and stored in a glovebox. Zn-oleate was made in a similar manner by adding together zinc acetate (0.16 g), OA (1 g), ODE (1.6 mL) and oleylamine (OLAM, 1.6 mL). The mixture was heated to 130°C and afterwards stored in a glovebox.

The growth of the CdS and ZnS shells is based on previous methods from Chen et al., Boldt et al. and Hanafi et al.[S1–S3] First, the CdS shell was grown. The CdSe cores (50 nmol) and ODE (3 mL) were added to a 100 mL three-neck flask and subsequently degassed. The temperature was raised to 310°C. At 240°C, Cd-oleate and 1-octanethiol (0.075 M in ODE) were injected slowly to grow a CdS shell at a rate of 1 monolayer per hour until a final thickness of 8 monolayers. The CdSe/CdS QDs were degassed at 120°C before growing the final ZnS shells.

To grow the ZnS shells, the QD solution was heated to 280°C. At 210°C, Zn-oleate and 1-octanethiol (0.55 M in ODE) were injected to grow a total of 2 monolayers of ZnS shell at a rate of 1 monolayer ZnS per hour. The product was washed twice with a methanol:butanol mixture (1:2), centrifuged, washed again with methyl acetate, which was followed by another centrifugation step. Finally, the QD solution was stored in a glovebox.

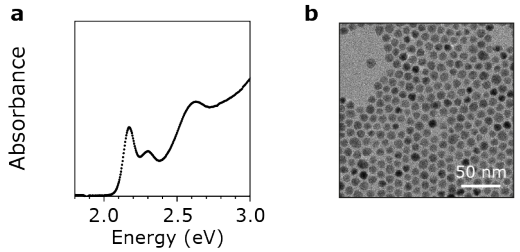

Figure S1 | Characterization of quantum dot sample. (a) Absorption spectrum of the CdSe cores used as seeds for the CdS/ZnS shell growth. From the spectral position of the 1S absorption (571 nm), we obtain an average core size of 1.84 nm using a sizing curve.[S4] **(b)** Transmission electron micrograph of the CdSe/CdS/ZnS core–shell–shell sample used in all experiments in this Letter. We measure 4.6 ± 0.4 nm (over 100 QDs) for the total QD radius. As we aimed at growing 8 monolayers of CdS and 2 monolayers of ZnS, we assume that 80% of the shell thickness is due to CdS. Hence, we estimate a radius of 4.1 ± 0.4 nm for the CdSe/CdS core–inner-shell part. The electron microscopy images were acquired with a JEOL JEM-1400 plus transmission electron microscope.

S2 Experimental setup

All single-QD measurements and ensemble time-resolved emission measurements were performed on a home-built optical setup consisting of a Nikon Ti-U inverted microscope body. The single-QD samples were prepared by spincoating a diluted (10^4 dilution factor) solution of QDs on a glass coverslip, which was then placed on the microscope. A 405-nm pulsed laser (Picoquant D-C 405, controlled by Picoquant PDL 800-D laser driver) was guided to the sample by a dichroic mirror (edge at 425 nm, Thorlabs DMLP425R) and focused by an oil-immersion objective (Nikon CFI Plan Apochromat Lambda 100×, NA 1.45) onto the sample. The QD emission was collected by the same objective and guided to two single-photon detectors in a Hanbury Brown–Twiss setup. The emission was split by a non-polarizing beamsplitter (Thorlabs BS013) and focused (achromatic aspherized lens Edmund optics, 49-659) onto an avalanche photodiode (APD; Micro Photonic Devices PDM, low dark counts <5 Hz) or guided to the galvo-APD setup.

The galvo-APD setup consists of a rotating galvo mirror (Thorlabs GVS011), whose angular position is linearly dependent on the input voltage (0.5 V/°). A sawtooth voltage profile with a typical repetition rate of 0.5–1 Hz (Agilent function generator) was used to periodically vary the angular position of the galvo mirror. We used a Thorlabs transmission grating for the ensemble time-resolved emission spectra (Figure 1 of the main text, 300 lines/mm GT25-03) and an Edmund transmission grating for the single-QD measurements (Figures 2–4 of the main text, 70 lines/mm 46-068).

The function generator, both APDs, and the laser driver were connected to a quTools quTAG time-to-digital converter, which communicated all photon detection events, laser pulses, and galvo-mirror sync pulses to a computer. Home-written software was used for live data visualization (e.g. photon-correlation function) and data storage.[S5]

For the single-QD measurements excitation powers between 10–20 nW were used at a repetition rate of 2.5 MHz. Using the absorption cross section obtained from fitting the power-dependent decay curves ($\sigma = 9.5 \times 10^{-15}$ cm^2) we obtained an average excitons per pulse n between 0.1–0.2 (to avoid significant contributions of multiexcitons other than biexcitons).

The QDs that were selected for their low-energy exciton emission (Figure 4a and Figure S8) were found using a separate spectrometer (Andor Kymera 193i, 150 lines/mm reflective grating) with a electron-multiplying CCD detector (Andor iXon Ultra 888).

S2.1 Resolution and calibration of galvo-APD setup

Figure 1a in the main text shows a schematic representation of the galvo-APD setup. Fourier imaging of the grating plane (first diffraction order) projects a range of detection wavelengths $\Delta\lambda$ onto the APD (detector size $a = 20$ µm). Periodically varying the angle of the galvo mirror varies the center detection wavelength λ_{det}. We can estimate the resolution, i.e. range of detection wavelengths $\Delta\lambda$ measured at any one time, of the galvo APD using a ray-transfer-matrix description of the optical elements between the grating and the detector. More specifically, we calculate the

position and angle (x, θ) with respect to the optical axis in the APD plane for a ray coming from (x_0, θ_0) in the grating plane by

$$\begin{pmatrix} x \\ \theta \end{pmatrix} = \begin{pmatrix} f\theta_0 \\ -x_0/f \end{pmatrix}. \tag{1}$$

The position in the APD plane x is indeed only dependent on the the outgoing angle θ_0 (and not x_0) and the focal distance of the lens f, characteristic for Fourier imaging. For a transmission grating we can relate the outgoing angle θ_0 to the wavelength of the outgoing photon by $\theta_0 \approx \lambda/L$, where L is the distance between the grating grooves. Using this, eq 1, and the detector size $\Delta x = a$, we arrive at a resolution

$$\Delta\lambda = \frac{aL}{f}, \tag{2}$$

which is dependent on the grating groove spacing (L), the lens focal distance (f) and the size of the APD active area (a).

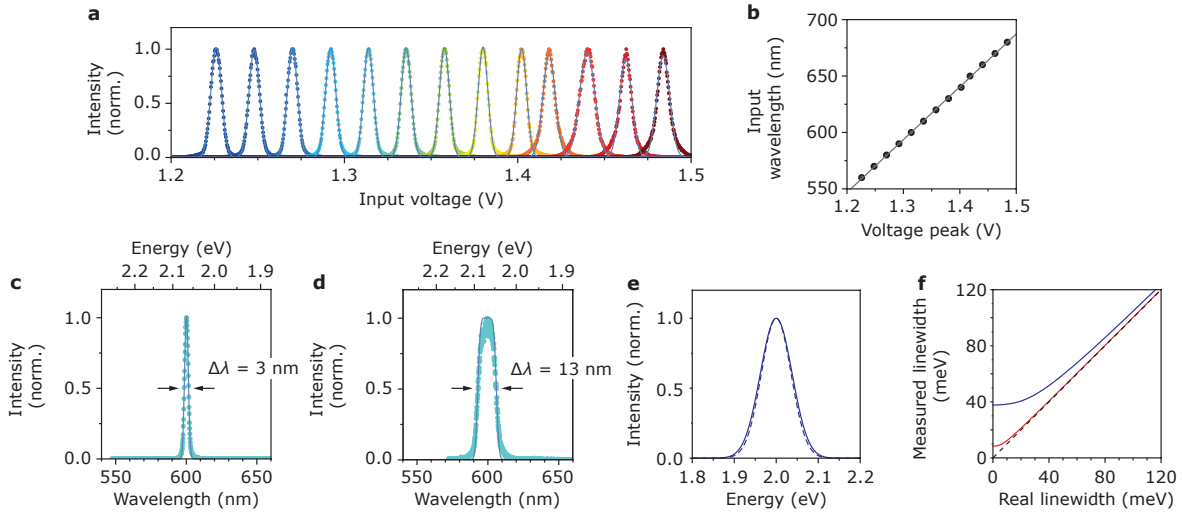

Figure S2 | Calibration of galvo-APD setup. The galvo-APD setup was calibrated using the reflection of a white-light laser (NKT Fianium FIU) in combination with a tunable filter (NKT LLTF Contrast, linewidth 1 nm). **(a)** Galvo-APD scans for 13 laser reflection wavelengths between 560 nm (blue) and 680 nm (red) using a sawtooth voltage profile with a peak-to-peak voltage of $V_{PP} = 320$ mV. The intensity detected by the galvo-APD is high for input voltages for which the detection energy E_{det} matches the laser wavelength. We fit all galvo-APD scans (solid lines) to obtain the voltage peak V for each input wavelength. **(b)** Input wavelength versus voltage peak (fitted from panel **a**). A linear fit to the data points serves as a calibration curve for the time-resolved emission measurements. Similar calibration measurements were done for the single-QD measurements, which used a different grating. **(c)** Calibrated galvo-APD scan of a laser reflection at 600 nm using a transmission grating with 300 lines/mm. We fit a model to the data points (solid line) that includes broadening [convolution of Gaussian function with boxcar function, $I(\lambda) * \Pi(\lambda, \Delta\lambda)$] of the spectrum of the laser $I(\lambda)$ by the detector resolution $\Delta\lambda = 3$ nm. **(d)** Same as in **c**, except we use the 70 lines/mm grating used for the single-QD measurements. We fit a detector resolution of $\Delta\lambda = 13$ nm, significantly smaller than the QD emission linewidth. The QD emission linewidths reported in the main text are corrected for detector broadening. **(e)** Simulated single-QD spectrum (dashed, input linewidth 83 meV) and measured spectrum (solid, measured linewidth 89 meV) after broadening by the detector resolution of $\Delta\lambda = 13$ nm. **(f)** Input versus measured linewidth using a 70 lines/mm transmission grating (blue) and 300 lines/mm grating (red). The measured single-QD emission linewidths reported in the main text are corrected for detector broadening by inversion of these simulation results.

S3 Ensemble biexciton shift from time-resolved emission spectroscopy

Extracting a reliable quantitative value for the ensemble-scale biexciton shift $\bar{E}_\mathrm{b}$ is challenging because biexciton emission cannot be isolated from emission of single excitons or higher multi-excitons. Moreover, homogeneous and inhomogeneous broadening of emission and absorption bands often significantly exceeds the spectral shifts between single-exciton and biexciton.

We integrated the time-resolved emission spectroscopy (TRES) maps $y_i(\lambda, t)$ over emission wavelength λ to obtain wavelength-integrated photoluminescence decay curves $Y_i(t)$. Here, i is an index for the measurements at different excitation powers. We fitted the first 20 ns of the data $Y_1(t)$ measured at the lowest power ($i = 1$; pump fluence $J_1 = 0.3\ \mu\mathrm{J\ cm^{-2}}$) to single exponential decay and extracted the single-exciton lifetime of $\tau_\mathrm{X} = 24$ ns. We fitted the photoluminescence decay curves at higher powers to a biexponential model:

$$Y_i(t) = A_i \left[P(\geq 1, \sigma J_i/\hbar\omega)\, \mathrm{e}^{-t/\tau_\mathrm{X}} + 4P(\geq 2, \sigma J_i/\hbar\omega)\, \mathrm{e}^{-t/\tau_\mathrm{BX}} \right], \tag{3}$$

where $P(\geq X, \mu) = \sum_{n=X}^{\infty} P(n, \mu)$ is the Poisson probability of X or more excitations per pulse given an expectation value of μ (see eq 7). The factor 4 in the second term comes from statistical scaling of the radiative recombination rates of single exciton and biexciton.[S6] Simultaneous fitting of the three measurements at $J_{2,3,4} = 5.2, 12.1, 17.2\ \mu\mathrm{J\ cm^{-2}}$, with $\{A_i\}$, σ, and τ_BX as fit parameters, yielded $\sigma = 9.5 \times 10^{-15}\ \mathrm{cm^2}$ and $\tau_\mathrm{BX} = 1.9$ ns.

Next, we integrated the TRES maps over delay time t between 0–0.6 ns and converted the wavelength axis to energy, to obtain the early-time spectra $\tilde{Y}_i(E)$. The exciton energy $E_\mathrm{X} = 2.004$ eV and the linewidth of the exciton emission fwhm = 89 meV were determined by a fit of the early-time spectrum at the lowest power to a Gaussian. We fitted the spectra at higher powers to a sum of Gaussians:

$$\tilde{Y}_i(E) = \tilde{A}_i \left[P(\geq 1, \sigma J_i/\hbar\omega)\, F(\tau_\mathrm{X})\, \mathrm{e}^{-4\log 2 (E-E_\mathrm{X})^2/\mathrm{fwhm}^2} + 4P(\geq 2, \sigma J_i/\hbar\omega)\, F(\tau_\mathrm{BX})\, \mathrm{e}^{-4\log 2 (E-E_\mathrm{X}-\bar{E}_\mathrm{b})^2/\mathrm{fwhm}^2} \right], \tag{4}$$

where

$$F(\tau) = 1 - \mathrm{e}^{-(0.6\ \mathrm{ns})/\tau} \tag{5}$$

is the fraction of the emission with a lifetime τ that falls within the first 0.6 ns after photoexcitation. Simultaneous fitting of the three measurements at $J_{2,3,4} = 5.2, 12.1, 17.2\ \mu\mathrm{J\ cm^{-2}}$, with $\{\tilde{A}_i\}$ and $\bar{E}_\mathrm{b}$ as fit parameters, yielded $\bar{E}_\mathrm{b} = 14$ meV. Figure 2e in the main text shows $\tilde{Y}_1(E)$ and $\tilde{Y}_3(E)$.

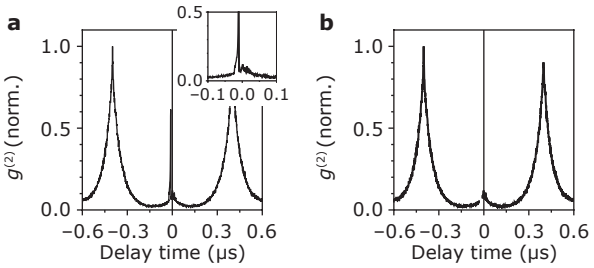

Figure S3 | Afterglow in photon-correlation experiments. Detector fluorescence, or afterglow, can show up in single-QD measurements using a Hanbury Brown–Twiss setup. Detection of a photon by one APD can trigger detector fluorescence, which then travels back to the sample, reflects off it, and is subsequently recorded by the other APD. In photon-correlation experiments, these events can show up in $g^{(2)}$ at delay times $\pm t'$, where t' is the time it takes for a photon to travel from one APD to the other APD. **(a)** Photon-correlation function $g^{(2)}$ from a single-QD experiment using the cascade-spectroscopy setup. We observe afterglow detection events for delay times $t = [-25, -10]$ ns (see inset for zoom-in) The absence of afterglow events for positive delay times indicates a low detection efficiency by the regular APD of afterglow photons originating from the galvo APD.**(b)** In all photon-correlations functions $g^{(2)}$ or energy-resolved $g^{(2)}$ in the main text, the afterglow events are not shown, by excluding the data points at delay times $t = [-25, -10]$ ns. The afterglow events contribute to the region highlighted 0^- in the correlation function of Figure 2b in the main text. We do not use this region for our analysis of the biexciton shift and biexciton emission spectrum, so our analysis is not affected by afterglow.

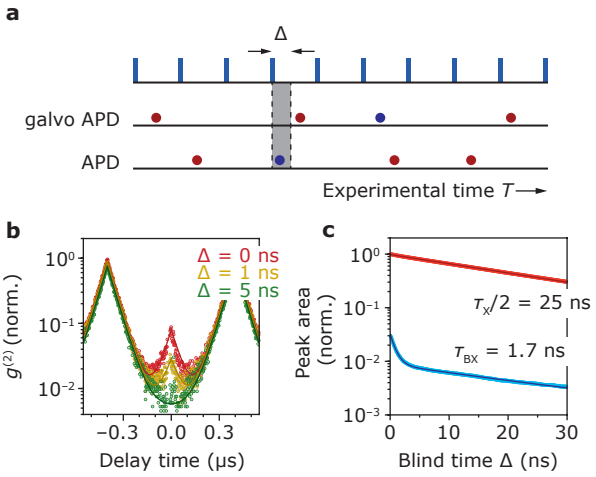

Figure S4 | Blind-time analysis We perform a blind-time analysis introduced by Deutsch et al.[S7] to warrant the contribution of biexciton cascade events to the zero-delay peak. **(a)** Schematic of the photon stream detected in a single-QD experiment. Laser pulses (blue vertical lines) arrive at the QD at regular intervals. The galvo-APD and the regular APD sometimes record photon arrivals (dots). We reject photons from the stream within a variable blind time Δ from the laser pulse, before using all other photon detection events to construct the intensity correlation function. **(b)** The normalized intensity correlation function $g^{(2)}$ for different values of Δ of 0 (red), 1 (yellow), and 5 (green) ns. Biexciton photons are more strongly affected by blind-time rejection than exciton photons. Hence, the decreasing zero-delay peak amplitude with increasing Δ proves that the zero-delay peak is due to biexciton cascades.[S8] **(c)** The decay of the peak area of zero-delay peak (blue; focus on the fast component) and side peaks (red) reveals the exciton and biexciton lifetimes of the QD. We extract values of $\tau_X = 50$ ns and $\tau_{BX} = 1.7$ ns. Assuming statistical scaling[S8] and that the exciton efficiency is $\eta_X = 1$, these lifetime values would correspond to a estimated biexciton efficiency of $\eta_{BX} = 0.13$. This estimate is consistent with the peak area ratio of $(N_0^- + N_0^+)/N_1 = 0.12$, furthering strengthening our interpretation that the zero-delay peak is due to biexciton cascades.

S4 Energy-resolved cross correlation

S4.1 Photon pair detection: events of types 1^-, 0^-, 0^+ and 1^+

The number of excitons created in a QD by a short laser pulse of fluence J is subject to Poisson statistics with a mean

$$\mu = \frac{\sigma J}{\hbar\omega}, \tag{6}$$

where σ is the absorption cross-section of the QD at photon energy $\hbar\omega$. The probability that n excitons are created, is

$$P(n,\mu) = \frac{\mu^n \mathrm{e}^{-\mu}}{n!}. \tag{7}$$

Based on this we can calculate the expected number of events of types 1^-, 0^-, 0^+ and 1^+ (Figure 2c of the main text). These determine the number of coincidence counts in the zero-delay and side peaks in the conventional (Figure 2b of the main text) and energy-resolved (Figures 2d,e of the main text) correlation functions. The probability that a laser pulse leads to the emission of a photon from the exciton state is

$$p_1 = \eta_{\mathrm{X}}[1 - P(0,\mu)], \tag{8}$$

where η_{X} is the exciton quantum yield, while the probability that it leads to a biexciton cascade is

$$p_2 = \eta_{\mathrm{BX}}\eta_{\mathrm{X}}[1 - P(0,\mu) - P(1,\mu)], \tag{9}$$

where η_{BX} is the biexciton quantum yield.

We assume that the emission spectra of exciton and biexciton are sufficiently similar that the detection efficiencies η_{det} for exciton and biexciton photons on the *regular* APD are the same. They are determined by the optics of the setup, by the 50/50 beam splitter, and by the properties of the detector itself. In contrast, the detection efficiencies, $\eta'_{\mathrm{det,BX}}$ and $\eta'_{\mathrm{det,X}}$, on the *galvo* APD are different and dependent on the set detection wavelength λ_{det}:

$$\eta'_{\mathrm{det},i}(\lambda_{\mathrm{det}}) = \eta_{\mathrm{det}} \int_{\lambda_{\mathrm{det}}-\Delta\lambda/2}^{\lambda_{\mathrm{det}}+\Delta\lambda/2} I_i(\lambda)\,\mathrm{d}\lambda, \tag{10}$$

where $I_i(\lambda)$ are the normalized exciton (i = X) and biexciton (i = BX) emission spectra and $\Delta\lambda$ is the spectral resolution of the setup. If $\Delta\lambda$ is much smaller than the spectral linewidth, we can approximate this to

$$\eta'_{\mathrm{det}}(\lambda_{\mathrm{det}}) \approx \eta_{\mathrm{det}} I_i(\lambda_{\mathrm{det}})\Delta\lambda = \tilde{\eta}_{\mathrm{det}} I_i(\lambda_{\mathrm{det}}), \tag{11}$$

where in the second step we have defined $\tilde{\eta}_{\mathrm{det}} = \eta_{\mathrm{det}}\Delta\lambda$.

The side peak in the correlation function centered at $t = -t_{\mathrm{rep}}$ (delay time equals minus a laser repetition period) counts the number N_1^- of events of type 1^-. These are due to two photons following consecutive laser pulses, where the first photon is detected on the regular APD and the second photon on the galvo APD. In the limit of weak excitation ($\mu \ll 1$), both of these photons are mostly *exciton* photons because biexciton emission is much less likely. At higher excitation fluences biexciton–exciton events will start to contribute to the side peak and multiexcitons other than biexcitons to the zero-delay peak. The expected number of events of type 1^- is then

$$N_1^- = \frac{T_{\mathrm{tot}}}{t_{\mathrm{rep}}} \times p_1\eta_{\mathrm{det}} \times p_1\tilde{\eta}_{\mathrm{det}} I_{\mathrm{X}}(\lambda_{\mathrm{det}}), \tag{12}$$

where T_{tot} is the total experiment time. In this expression, the second factor is the probability that a first laser pulse leads to an exciton photon and the regular APD detects it; the third factor is the probability that the next following laser pulse leads to a second exciton photon and the galvo APD detects it. Similar considerations lead to expressions

for the number of events of type 0^-, N_0^-, of type 0^+, N_0^+, and of type 1^+, N_1^+:

$$N_1^- = \frac{T_{\rm tot}}{t_{\rm rep}} \tilde{\eta}_{\rm det} \eta_{\rm det} p_1^2 I_{\rm X}(\lambda_{\rm det}) \tag{13}$$

$$N_0^- = \frac{T_{\rm tot}}{t_{\rm rep}} \tilde{\eta}_{\rm det} \eta_{\rm det} p_2 I_{\rm X}(\lambda_{\rm det}) \tag{14}$$

$$N_0^+ = \frac{T_{\rm tot}}{t_{\rm rep}} \tilde{\eta}_{\rm det} \eta_{\rm det} p_2 I_{\rm BX}(\lambda_{\rm det}) \tag{15}$$

$$N_1^+ = \frac{T_{\rm tot}}{t_{\rm rep}} \tilde{\eta}_{\rm det} \eta_{\rm det} p_1^2 I_{\rm X}(\lambda_{\rm det}) \tag{16}$$

We see that $N_1^- = N_1^+ = N_1$. In the limit of weak excitation we have $p_1^2 \approx \eta_{\rm X}^2 \mu^2$ and $p_2 \approx \frac{1}{2}\eta_{\rm BX}\eta_{\rm X}\mu^2$. The *ratios* of peak areas in the correlation function then reduce to the expressions we use in the main text (Figure 2 and eqs 1,2):

$$\frac{N_0^+ + N_0^-}{N_1} = \frac{\eta_{\rm BX}}{\eta_{\rm X}} \tag{17}$$

$$\frac{N_0^+}{N_1} = \frac{1}{2}\frac{\eta_{\rm BX}}{\eta_{\rm X}}\frac{I_{\rm BX}(\lambda_{\rm det})}{I_{\rm X}(\lambda_{\rm det})} \tag{18}$$

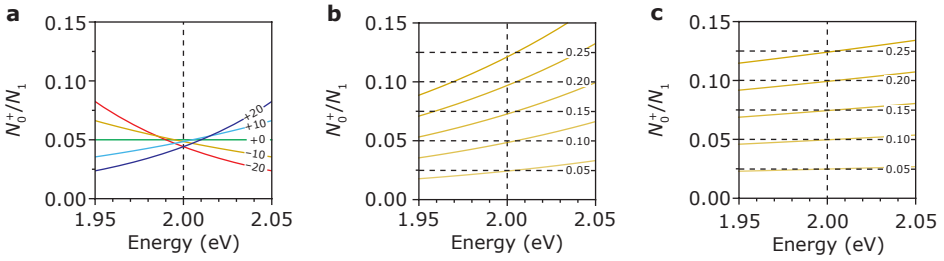

Figure S5 | Energy-resolved $g^{(2)}$ **(a)** Calculated ratio N_0^+/N_1 (eq 26) as a function of galvo-APD detection energy $E_{\rm det}$ for a QD with $\eta_{\rm BX}/\eta_{\rm X} = 0.1$ and different biexciton shift $E_{\rm b}$, ranging from biexciton binding (red; $E_{\rm b} = -20$ meV) to biexciton repulsion (blue; $E_{\rm b} = +20$ meV). The emission spectra of exciton and biexciton are assumed to be Gaussian with equal widths fwhm $= 94.2$ meV and to peak at $E_{\rm X} = 2.00$ eV and $E_{\rm BX} = 2.00$ eV $+ E_{\rm b}$, respectively. **(b)** Calculations similar to those in panel **a**, but $E_{\rm b}$ is fixed at a value of $+10$ meV and $\eta_{\rm BX}/\eta_{\rm X}$ is varied in between 0.05 and 0.25. **(c)** Calculations similar to those in panel **b**, but $E_{\rm b}$ is fixed at a value of $+10$ meV and the linewidth is increased to fwhm $= 188.4$ meV.

In Figure 2 of the main text and Figure S5, we extract the biexciton shift $E_{\rm b} = E_{\rm BX} - E_{\rm X}$ from the dependence of the ratio N_0^+/N_1 on the galvo-APD detection energy $E_{\rm det}$. The direction in which the curve slopes immediately reveals whether the biexciton is repulsive ($E_{\rm b} > 0$) or attractive ($E_{\rm b} < 0$). For our analysis, we assume that the exciton and biexciton emission spectra are both Gaussian with equal standard deviations σ. In the limit that $|E_{\rm b}| \ll \sigma$—which is the case for all our QDs—expansion of eq 18,

$$\frac{N_0^+}{N_1} = \frac{1}{2}\frac{\eta_{\rm BX}}{\eta_{\rm X}} + \frac{E_{\rm b}}{2\sigma^2}\frac{\eta_{\rm BX}}{\eta_{\rm X}}(E_{\rm det} - E_{\rm X}) + \mathcal{O}\left[(E_{\rm det} - E_{\rm X})^2\right], \tag{19}$$

reveals that the slope of the curve near the emission peak maximum is directly proportional to the biexciton shift $E_{\rm b}$. This makes it possible to rapidly identify the QDs with the strongest biexciton shift from the plots in Figure S5.

S4.2 Integrating over a long experiment

Integrating a photon-correlation experiment over a long experiment of many periods of the galvo mirror reproduces a 'regular' $g^{(2)}$ plot. As the galvo mirror angle follows a sawtooth profile in time, integrating over the experiment is

equivalent to averaging over detection wavelength. Averaged over λ_{det}, eqs 13–16 become

$$\langle N_1^- \rangle = \frac{T_{\mathrm{tot}}}{t_{\mathrm{rep}}} \eta_{\mathrm{det}}^2 p_1^2 \frac{\Delta\lambda}{\Lambda} \tag{20}$$

$$\langle N_0^- \rangle = \frac{T_{\mathrm{tot}}}{t_{\mathrm{rep}}} \eta_{\mathrm{det}}^2 p_2 \frac{\Delta\lambda}{\Lambda} \tag{21}$$

$$\langle N_0^+ \rangle = \frac{T_{\mathrm{tot}}}{t_{\mathrm{rep}}} \eta_{\mathrm{det}}^2 p_2 \frac{\Delta\lambda}{\Lambda} \tag{22}$$

$$\langle N_1^+ \rangle = \frac{T_{\mathrm{tot}}}{t_{\mathrm{rep}}} \eta_{\mathrm{det}}^2 p_1^2 \frac{\Delta\lambda}{\Lambda} \tag{23}$$

These are the regular expressions for a HBT experiment but modified with a factor $\Delta\lambda/\Lambda$ which accounts for the fraction of the full spectral range scanned Λ that is recorded by the galvo APD at any one time.

S4.3 Including dark counts

We include the effect of dark counts on the peak area ratio with a parameter d, which is the probability that a detector registers a dark count following a laser pulse. We assume equal d for the two detectors. Including this term in eq 12 yields

$$N_1^- = \frac{T_{\mathrm{tot}}}{t_{\mathrm{rep}}} \times \left(p_1 \eta_{\mathrm{det}} + d\right) \times \left[p_1 \tilde{\eta}_{\mathrm{det}} I_{\mathrm{X}}(\lambda_{\mathrm{det}}) + d\right] \tag{24}$$

Similar procedure yields expressions for N_0^-, N_0^+, and N_1^+. As we use low-dark-count detectors and low excitation fluences, we can neglect all terms of order d^2 or higher, $\mu^2 d$ or higher, and μ^3 or higher. We arrive at

$$\frac{N_0^-}{N_1} = \frac{\frac{1}{2}\mu\tilde{\eta}_{\mathrm{det}}\eta_{\mathrm{X}} I_{\mathrm{BX}} + \left(\eta_{\mathrm{det}} + \tilde{\eta}_{\mathrm{det}} I_{\mathrm{X}}\right) d}{\mu\tilde{\eta}_{\mathrm{det}}\eta_{\mathrm{X}} I_{\mathrm{X}} + \left(\eta_{\mathrm{det}} + \tilde{\eta}_{\mathrm{det}} I_{\mathrm{X}}\right) d} \tag{25}$$

$$\frac{N_0^+}{N_1} = \frac{\frac{1}{2}\mu\tilde{\eta}_{\mathrm{det}}\eta_{\mathrm{BX}} I_{\mathrm{BX}} + \left(\eta_{\mathrm{det}} + \tilde{\eta}_{\mathrm{det}} I_{\mathrm{X}}\right) d}{\mu\tilde{\eta}_{\mathrm{det}}\eta_{\mathrm{X}} I_{\mathrm{X}} + \left(\eta_{\mathrm{det}} + \tilde{\eta}_{\mathrm{det}} I_{\mathrm{X}}\right) d} \tag{26}$$

where I_{BX} and I_{X} are evaluated at λ_{det}. The ratio N_0^-/N_1 approaches a value of 1 as $I_{\mathrm{BX}}(E_{\mathrm{det}})$ and $I_{\mathrm{BX}}(E_{\mathrm{det}})$ go to zero at the tails of the emission band, which is consistent with our experimental observations (Figure 2f of the main text). Eqs 25, 26 reduce to eqs 17, 18 if we let d go to zero.

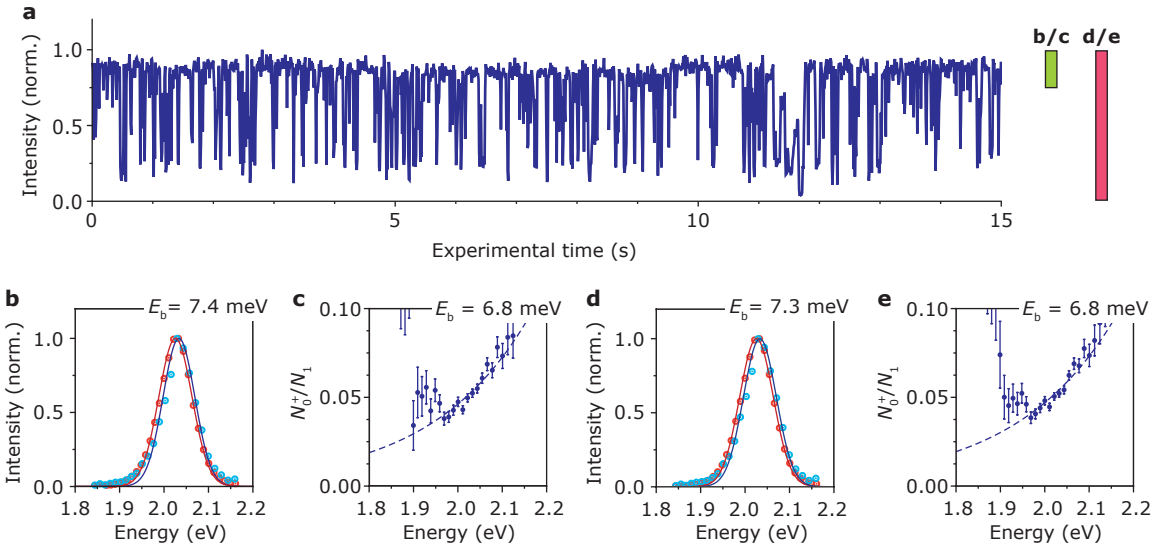

Figure S6 | Influence of intermittent gray state on extracted biexciton shift. **(a)** Intensity trace of single quantum dot (same as Figures 2b–f and Figure 3a) showing intermittent switching between a high-intensity bright state and a low-intensity gray state. Green (b,c) and red (d,e) intensity ranges are used to construct the exciton/biexciton emission spectra in b,d and the N_0^+/N_1 ratio in c,e. **(b)** Reconstructed exciton (N_1) and biexciton (N_0^+) spectrum using the intensity thresholdig from a (green) to discard the intermittent gray state. We extract a single-QD biexciton shift of $E_b = 7.4$ meV. **(c)** N_0^+/N_1 as a function of E_{det} using the intensity thresholding from a (green) to discard the intermittent gray state. We extract a single-QD biexciton shift of $E_b = 6.8$ meV. **(d,e)** Same as b,c but without intensity thresholding. We observe minimal influence of thresholding on the value extracted for the biexciton shift.

S5 Perturbation theory calculations

We construct a simple model for the exciton and biexciton energies in core–shell QDs. It uses the particle-in-a-spherical-box model for the electron and hole levels and includes Coulomb interactions between the carriers in the (bi)exciton as a perturbation up to second order.

We assume that holes are confined to the CdSe core of radius a and particle-in-a-spherical-box levels with single-particle wave function $\psi(\mathbf{r}_h)$. In our model, the electrons are delocalized over the CdSe core and the CdS shell with no potential step between the core and shell, while the potential step with the outer ZnS shell is infinitely high. Consequently, the single-particle wave functions $\varphi(\mathbf{r}_e)$ of the electron are also particle-in-a-spherical-box functions, but confined to a larger sphere of radius b (= CdSe core + CdS shell).

The exciton states are written as a product of single-particle wave functions. The lowest-energy exciton state $\Psi_{X,0}$ is

$$\Psi_{X,0}(\mathbf{r}_e, \mathbf{r}_h) = \psi_{1S}(\mathbf{r}_h)\varphi_{1S}(\mathbf{r}_e), \tag{27}$$

where subscripts 1S denote the lowest-energy single-particle levels. The excited exciton states $\Psi_{X,i}$ are built from different combinations of single-particle levels. We construct biexciton states from four single-particle levels. In the biexciton ground state, the pair of electrons and the pair of holes all occupy 1S levels with their spins paired:

$$\Psi_{BX,0}(\mathbf{r}_{e1}, \mathbf{r}_{e2}, \mathbf{r}_{h1}, \mathbf{r}_{h2}) = \frac{1}{2}\left[\psi_{1S}(\mathbf{r}_{h1})\bar{\psi}_{1S}(\mathbf{r}_{h2}) - \bar{\psi}_{1S}(\mathbf{r}_{h1})\psi_{1S}(\mathbf{r}_{h2})\right]\left[\varphi_{1S}(\mathbf{r}_{e1})\bar{\varphi}_{1S}(\mathbf{r}_{e2}) - \bar{\varphi}_{1S}(\mathbf{r}_{e1})\varphi_{1S}(\mathbf{r}_{e2})\right]. \tag{28}$$

Here, single-particle levels with and without bar, e.g. ψ and $\bar{\psi}$, denote the two possible spin orientations. The excited biexciton states $\Psi_{BX,i}$ are built from different combinations of single-particle levels. Only states with paired electron and paired hole spins are relevant for our perturbation corrections to the energy of the biexciton ground state.

In our calculations of the exciton and biexciton energies, we treat Coulomb interactions between the carriers as a perturbation. The zeroth-order energies $E^{(0)}$, including only confinement energy, are

$$E^{(0)}_{\mathrm{X},0} = E_\mathrm{g} + \frac{\hbar^2\pi^2}{2m_\mathrm{h}a^2} + \frac{\hbar^2\pi^2}{2m_\mathrm{e}b^2}. \tag{29}$$

for the exciton ground state and

$$E^{(0)}_{\mathrm{BX},0} = 2E_\mathrm{g} + 2\frac{\hbar^2\pi^2}{2m_\mathrm{h}a^2} + 2\frac{\hbar^2\pi^2}{2m_\mathrm{e}b^2}. \tag{30}$$

for the biexciton ground state. Here, $E_\mathrm{g} = 1.74$ eV is the bulk bandgap and $m_\mathrm{h} = 1.0m_0$ and $m_\mathrm{e} = 0.1m_0$ (with m_0 the electron rest mass in vacuum) are the effective hole and electron masses in CdSe.[S9] The zeroth-order energies of the excited exciton and biexciton states, $E^{(0)}_{\mathrm{X},i}$ and $E^{(0)}_{\mathrm{BX},i}$, are similarly given by the particle-in-a-spherical-box model. Including Coulomb interactions between carriers up to second order, the energies of exciton and biexciton ground state become

$$E_{\mathrm{X},0} = E^{(0)}_{\mathrm{X},0} + \langle\Psi_{\mathrm{X},0}|V|\Psi_{\mathrm{X},0}\rangle + \sum_i \frac{|\langle\Psi_{\mathrm{X},0}|V|\Psi_{\mathrm{X},i}\rangle|^2}{E^{(0)}_{\mathrm{X},0} - E^{(0)}_{\mathrm{X},i}} \tag{31}$$

$$E_{\mathrm{BX},0} = E^{(0)}_{\mathrm{BX},0} + \langle\Psi_{\mathrm{BX},0}|V|\Psi_{\mathrm{BX},0}\rangle + \sum_i \frac{|\langle\Psi_{\mathrm{BX},0}|V|\Psi_{\mathrm{BX},i}\rangle|^2}{E^{(0)}_{\mathrm{BX},0} - E^{(0)}_{\mathrm{BX},i}}. \tag{32}$$

Here, V is the Coulomb operator, which includes attractions between all pairs unlike carriers and repulsion between pairs of like carriers. The summations i run over all possible excited states that can be constructed with the basis set of single-particle levels. To prevent that the four-carrier calculations become too involved, we use a limited basis set including only 1S, 1P and 2S.

The biexciton binding energy is defined as $E_\mathrm{b} = E_{\mathrm{BX},0} - 2E_{\mathrm{X},0}$. The energy of the biexciton $\rightarrow$ exciton emission is $E_{\mathrm{BX},0} - E_{\mathrm{X},0}$. In the main text (Figure 4b) we present the calculated ground-state exciton energies $E_{\mathrm{X},0}$ and the biexciton binding E_b for CdSe core radii a and CdSe/CdS core–shell radii b.

S5.1 Scaling of Coulomb integrals with QD geometry

For the intuitive discussion accompanying eqs 3–6 of the main text, we use analytical expressions for the Coulomb integrals between core-localized 1S hole and core–shell-extended 1S electrons. Each of the Coulomb integrals J_{ij} between carriers i and j is of the form

$$J_{ij} = \frac{q_i q_j}{4\pi\varepsilon\varepsilon_0}\int_{V_j}\int_{V_i}\frac{|\chi_i|^2|\chi_j|^2}{|\mathbf{r}_i - \mathbf{r}_j|}\mathrm{d}\mathbf{r}_i\mathrm{d}\mathbf{r}_j, \tag{33}$$

where q_i is the charge of carrier i, χ_i is the corresponding 1S single-carrier orbital, and V_i the total volume it occupies. The Coulomb integrals between like carriers have analytical expressions with a numerical prefactor:

$$J_{\mathrm{ee}} \approx +1.79\,\frac{e^2}{4\pi\varepsilon\varepsilon_0 b}, \tag{34}$$

$$J_{\mathrm{hh}} \approx +1.79\,\frac{e^2}{4\pi\varepsilon\varepsilon_0 a}. \tag{35}$$

The Coulomb attraction between electron and hole, which occupy different volumes, is more difficult. If we assume a thick shell ($b \gg a$) we can approximate the hole wave function by a delta function and the integral can again be analytically evaluated, yielding

$$J_{\mathrm{eh}} \approx -2.44\,\frac{e^2}{4\pi\varepsilon\varepsilon_0 b}. \tag{36}$$

S6 Extended data: N_0^+, N_1 and N_0^+/N_1 for all single-QD measurements

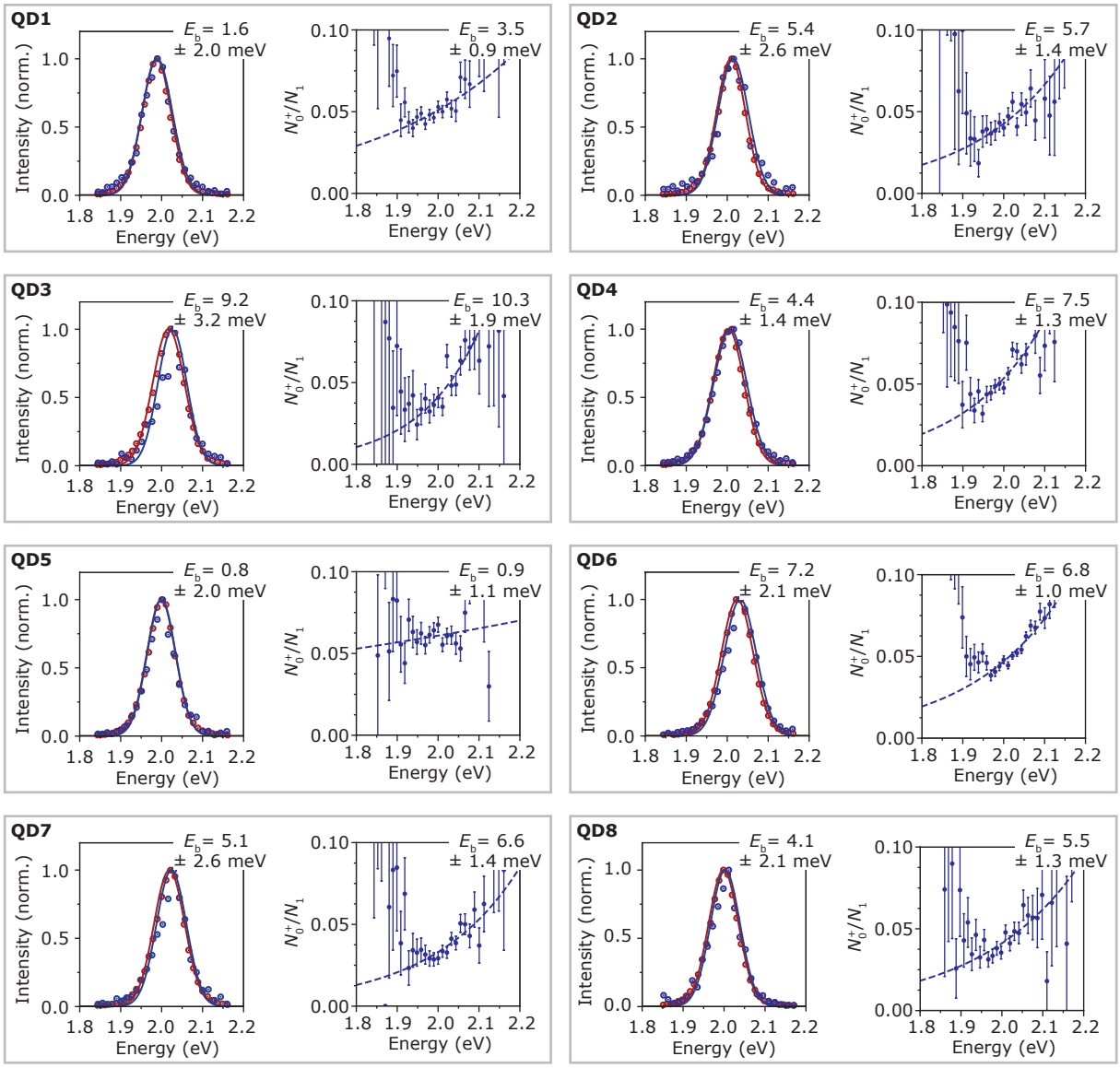

Figure S7 | For single QDs 1–8: Left, plots of N_0^+ (blue) and N_1 (red) as a function of detection energy; right, plot of N_0^+/N_1 as a function of detection energy. Error on biexciton shift ($\pm\sigma$) indicated for all measurements in inset.

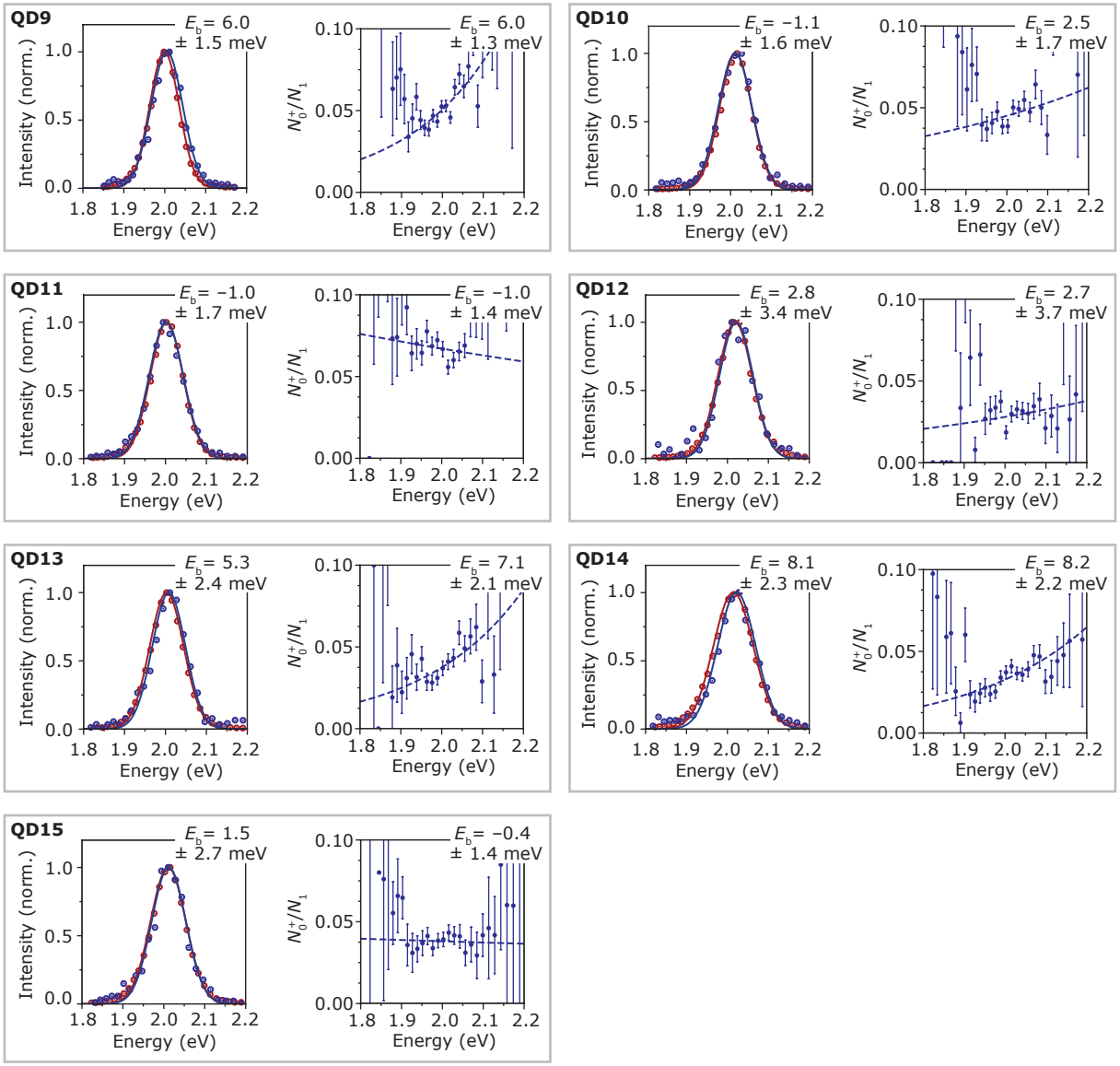

Figure S8 | For single QDs 9–15: Left, plots of N_0^+ (blue) and N_1 (red) as a function of detection energy; right, plot of N_0^+/N_1 as a function of detection energy.Error on biexciton shift ($\pm\sigma$) indicated for all measurements in inset.

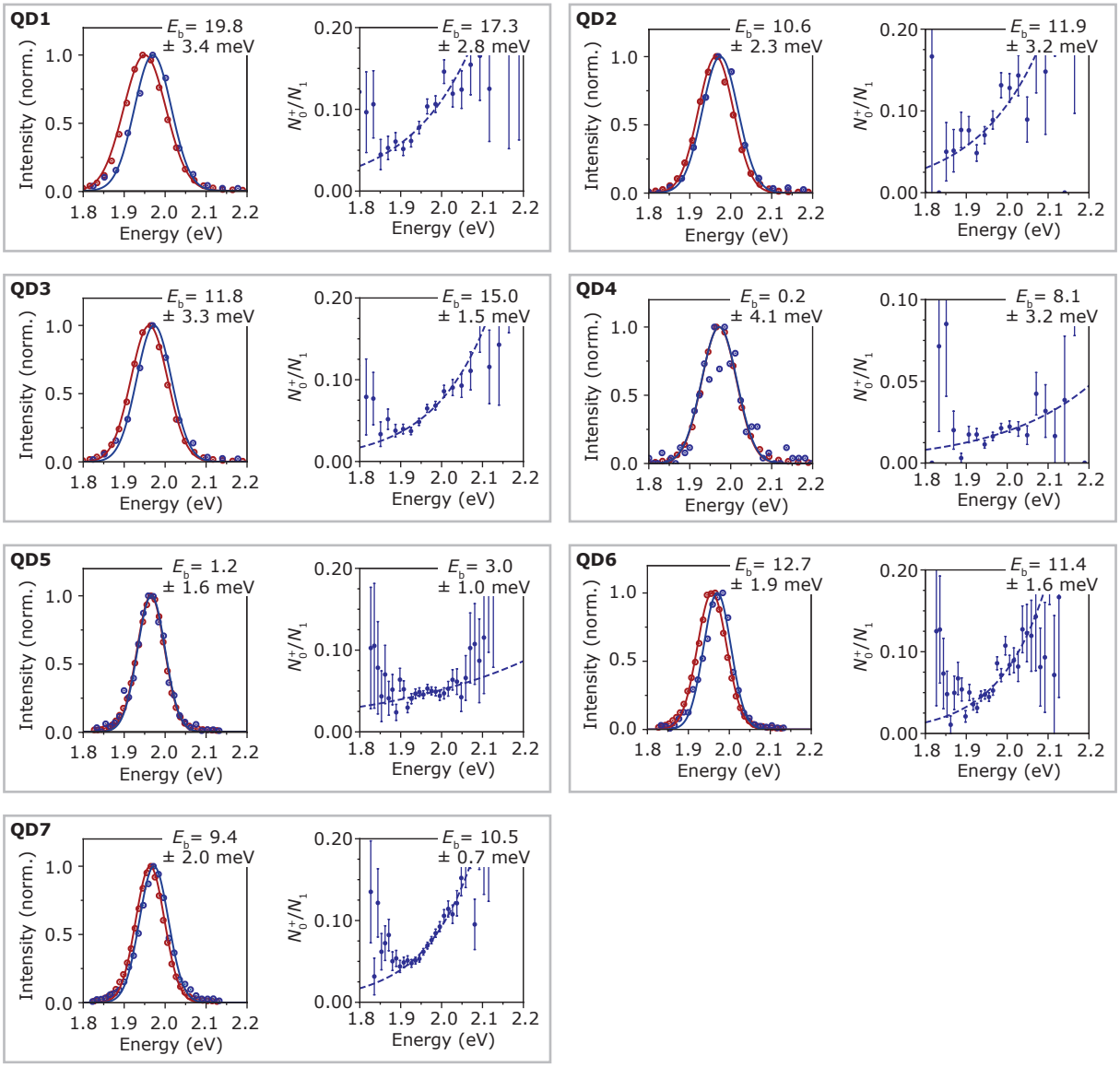

Figure S9 | For preselected single QDs 1–8 with low-energy exciton emission: Left, plots of N_0^+ (blue) and N_1 (red) as a function of detection energy; right, plot of N_0^+/N_1 as a function of detection energy. Error on biexciton shift ($\pm\sigma$) indicated for all measurements in inset.

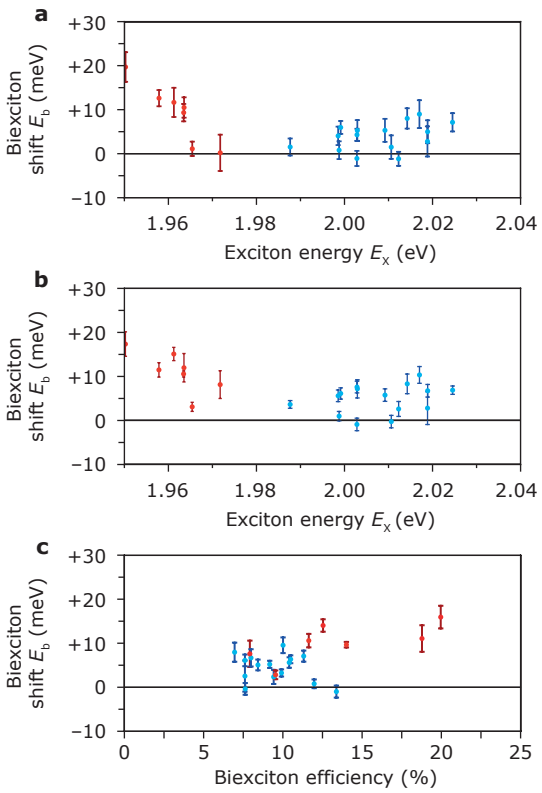

Figure S10 | Biexciton shift E_b, efficiency η_{BX} and exciton energy E_X of all single QDs (a) Biexciton shift vs. exciton energy for all QDs measured. Biexciton shift E_b is determined from N_0^+ vs. detection energy **(b)** Same as **(a)**, but biexciton shift determined from N_0^+/N_1 vs. detection energy E_{det} **(c)** Biexciton efficiency and E_b for all single QDs.

Supporting References

(S1) Chen, O.; Zhao, J.; Chauhan, V. P.; Cui, J.; Wong, C.; Harris, D.K.; Wei, H.; Han, H.S.; Fukumura, D.; Jain, R.K.; Bawendi, M.G. Compact high-quality CdSe–CdS core–shell nanocrystals with narrow emission linewidths and suppressed blinking, *Nat. Mater.* **2013**, *12*, 445–451.

(S2) Boldt, K.; Kirkwood, N.; Beane, G.A.; Mulvaney, P. Synthesis of highly luminescent and photo-stable, graded shell CdSe/$Cd_xZn_{1-x}S$ nanoparticles by in situ alloying, *Chem. Mater.* **2013**, *25*, 4731–4738.

(S3) Hanifi, D.A.; Bronstein, N.D.; Koscher, B.A.; Nett, Z.; Swabeck, J.K.; Takano, K.; Schwartzberg, A.M.; Maserati, L.; Vandewal, K.; van de Burgt, Y.; Salleo, A., Alivisatos, P.A. Redefining near-unity luminescence in quantum dots with photothermal threshold quantum yield, *Science* **2019**, *363*, 199–1202.

(S4) Jasieniak, J.; Smith, L.; van Embden, J.; Mulvaney, P. Re-examination of the size-dependent absorption properties of CdSe quantum dots, *J. Phys. Chem. C.* **2009**, *113*, 19468–19474.

(S5) Hinterding, S.O.M; Rabouw, F.T. PHoton Arrival-Time STudio (PHAST), *Zenodo* **2020** https://doi.org/10.5281/zenodo.4354144.

(S6) Galland, C.; Ghosh, Y.; Steinbrück, A.; Sykora, M; Hollingsworth, J.A.; Klimov, V.I.; Htoon, H. Two types of luminescence blinking revealed by spectroelectrochemistry of single quantum dots, *Nature* **2011**, *479*, 203–207.

(S7) Deutsch, Z.; Schwartz, O.; Tenne, R.; Popovitz–Biro, R.; Oron, D. Two-color antibunching from band-gap engineered colloidal semiconductor nanocrystals, *Nano Lett.* **2012**, *12*, 2948–2952.

(S8) Mangum, B.D.; Ghosh, Y.; Hollingsworth, J.A.; Htoon, H. Disentangling the effects of clustering and multiexciton emission in second-order photon correlation experiments, *Opt. Express* **2013**, *21*, 7419–7426.

(S9) De Mello Donega, C. Synthesis and properties of colloidal heteronanocrystals, *Chem. Soc. Rev.* **2011**, *40*, 1512–1546.